Steering of Multisegment Continuum Manipulators Using Rigid-Link Modeling and FBG-Based Shape Sensing

Roy J. Roesthuis, *Student Member, IEEE*, and Sarthak Misra, *Member, IEEE*

***Abstract*—Accurate closed-loop control of continuum manipulators requires integration of both models that describe their motion and methods to evaluate manipulator shape. This work presents a model that approximates the continuous shape of a continuum manipulator by a serial chain of rigid links, connected by flexible rotational joints. This rigid-link model permits a description of manipulator shape under different loading conditions. A kinematic controller, based on the manipulator Jacobian of the proposed rigid-link model, is implemented and realizes trajectory tracking, while using the kinematic redundancy of the manipulator to perform a secondary task of avoiding obstacles. The controller is evaluated on an experimental testbed, consisting of a planar tendon-driven continuum manipulator with two bending segments. Fiber Bragg grating (FBG) sensors are used to reconstruct 3-D manipulator shape, and is used as feedback for closed-loop control of the manipulator. Manipulator steering is evaluated for two cases: the first case involving steering around a static obstacle and the second case involving steering along a straight path while avoiding a moving obstacle. Mean trajectory tracking errors are 0.24 and 0.09 mm with maximum errors of 1.37 and 0.52 mm for the first and second cases, respectively. Finally, we demonstrate the possibility of FBG sensors to measure interaction forces, while simultaneously using them for shape sensing.**

***Index Terms*—Continuum manipulator, fiber Bragg gratings (FBG), force sensing, motion control, obstacle avoidance.**

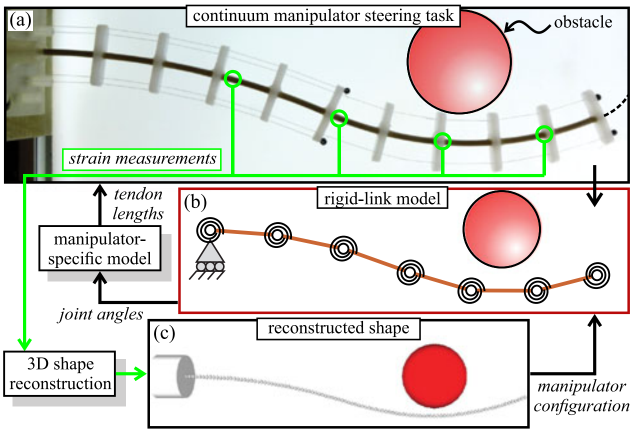

Fig. 1. (a) Due to the flexible nature of continuum manipulators, steering them is challenging: It requires both models that describe manipulator shape and methods to measure manipulator shape during steering. (b) In this work, we present a model that describes continuum manipulator shape by a serial chain of rigid links, connected by flexible, rotational joints. Joint angles are calculated by using the rigid-link model, and tendon lengths are calculated by using a manipulator-specific model. (c) Array of FBG sensors measure bending strain at several locations along the manipulator shaft. This is used to reconstruct 3-D manipulator shape, which is used to provide feedback of manipulator shape during steering.

I. Introduction

Continuum manipulators consist of an elastic structure, which allows them to bend along their length in a continuous manner [1]. Due to their inherent flexibility, continuum manipulators can operate safely within delicate environments such as the human body; hence, they have gained interest in research areas related to medicine [2]–[7]. Flexible continuum-style surgical instruments can reach locations in the human body that are inaccessible when using traditional straight devices. Examples of such instruments are steerable catheters for cardiac surgery [2], [5] and instruments for laryngeal surgery [3] and transurethral interventions [7]. Another example of continuum manipulators for minimally invasive surgery (MIS) procedures are concentric tube robots, which have been investigated for cardiac surgery and skull base surgery [4], [6].

Accurately steering continuum manipulators with multiple segments require models that describe the position and orientation (i.e., kinematics) of the manipulator upon actuation. A well-known method for describing the shape of continuum manipulators is the piecewise constant-curvature approach [1]. This approach assumes constant-curvature bending for each segment such that manipulator shape can be described by a series of constant-curvature arcs [1], [8]. The constant-curvature approach allows us to solve the inverse kinematics (IK) problem for continuum manipulators with multiple segments. Neppalli *et al.* presented a closed-form solution for the IK problem, assuming the end points of the segments are known [9]. In other studies, the IK problem was solved through the use of the manipulator Jacobian [10]–[13]. However, the constant-curvature approach has its limitations when external loads act

Manuscript received June 16, 2015; revised December 29, 2015; accepted January 12, 2016. Date of publication March 21, 2016; date of current version April 1, 2016. This paper was recommended for publication by Associate Editor R. J. Webster, III, and Editor B. J. Nelson upon evaluation of the reviewers' comments. This work was supported by the Dutch Technology Foundation STW under H-Haptics Project #12159, which is part of The Netherlands Organization for Scientific Research (NWO), and was partly funded by the Ministry of Economic Affairs, Agriculture and Innovation.

R. J. Roesthuis is with the Surgical Robotics Laboratory, Department of Biomechanical Engineering, and MIRA—Institute for Biomedical Technology and Technical Medicine, University of Twente, 7522 NB Enschede, The Netherlands (e-mail: r.j.roesthuis@utwente.nl).

S. Misra is with the Surgical Robotics Laboratory, Department of Biomechanical Engineering, and MIRA—Institute for Biomedical Technology and Technical Medicine, University of Twente, 7522 NB Enschede, The Netherlands, and also with the Department of Biomedical Engineering, University of Groningen and University Medical Centre Groningen, 9713 GZ Groningen, The Netherlands (e-mail: s.misra@utwente.nl).

This paper has supplementary downloadable material available at http://ieeexplore.ieee.org.

Color versions of one or more of the figures in this paper are available online at http://ieeexplore.ieee.org.

Digital Object Identifier 10.1109/TRO.2016.2527047

on the manipulator, in particular when they are not directed in the bending plane of the segments. In some scenarios, accurate knowledge of manipulator shape is required. In order to accurately describe manipulator shape under external loading, different studies have used the Cosserat rod model [14]–[16]. This model describes the manipulator as a thin elastic rod parameterized by the arc length. This description results in a boundary value problem, consisting of a set of nonlinear differential equations with boundary conditions, which depend on the loading conditions. Obtaining the manipulator Jacobian in an efficient way is challenging, due to the complexity of the kinematics. Jones *et al.* presented a method for obtaining the Jacobian using the Cosserat rod model by applying finite differences [15]. Rucker and Webster presented another method for computing the manipulator Jacobian in an indirect way by introducing an initial value Jacobian, which is either solved using finite differences or a derivative propagation approach [17].

In this work, we present a model that approximates the continuous shape of a continuum manipulator by a serial chain of rigid links, connected by flexible rotational joints. This rigid-link model can describe large manipulator deflections under external loading conditions. The kinematics are simplified compared with the Cosserat rod model, and the manipulator Jacobian can be derived in a straightforward manner. We show that the approximation by rigid links allows the description of manipulator shape in a precise way, which is comparable with the geometrically exact Cosserat rod model. We believe this modeling approach provides insight into the modeling of continuum manipulator under external loading conditions and offers further possibilities of intrinsic force sensing and force control when interacting with the environment [18].

A kinematic controller, which uses the manipulator Jacobian of the rigid-link model, is implemented and realizes trajectory tracking and obstacle avoidance. The controller calculates the joint angles [see Fig. 1(b)] and from these the tendon lengths are computed using a manipulator-specific model. The controller is evaluated on an experimental testbed for two different steering cases. The testbed consists of a planar tendon-driven manipulator with two segments [see Fig. 1(a)]. Manipulator shape is reconstructed using an array of fiber Bragg grating (FBG) sensors, and this is used both for model validation and closed-loop control [see Fig. 1(c)]. In a previous study, we have used an array of FBG sensors to determine the shape of a single-segment tendon-driven manipulator [19]. In this study, we also show that FBG sensors can be used to measure interaction forces at the manipulator tip, while simultaneously sensing manipulator shape.

This paper is organized as follows. In Section II, we present our rigid-link modeling approach of multisegment continuum manipulators. Section III discusses the steering of a tendon-driven manipulator, and shape sensing using FBG sensors is explained in Section IV. The experimental setup is described in Section V, followed by the experimental results in Section VI. Finally, we conclude this study in Section VII, in which we also provide directions for ongoing and future work.

II. Rigid-Link Modeling of Continuum Manipulators

This section presents the modeling of continuum manipulators using a rigid-link approximation. We first describe the kinematics, followed by shape calculation under external loading. Finally, we present the derivation of the manipulator Jacobian using the rigid-link model.

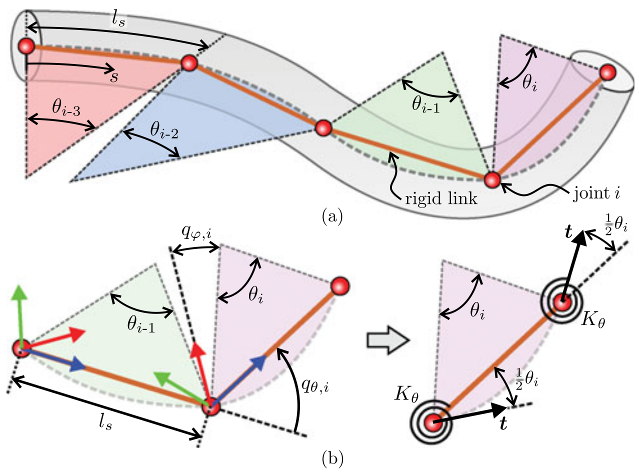

Fig. 2. (a) Three-dimensional shape of a continuum manipulator is approximated by a serial chain of rigid links, connected by rotational joints. Each link describes a constant-curvature arc of fixed length (l_s). Each arc is defined by a bend angle (θ_i) and a bending direction (φ_i). (b) Joint orientation is defined by two angles: The first angle ($q_{\varphi,i}$) is related to the bending direction, and the second angle ($q_{\theta,i}$) is related to the amount of bending. In order to model manipulator stiffness, a rotational spring (K_θ) is assigned to each joint.

A. Rigid-Link Kinematics of a Continuum Manipulator

Manipulators designed for clinical procedures are often slender, i.e., they are small in diameter compared with their length. In such cases, shear strains are small compared with bending strains. Hence, in the following derivation, we consider manipulator deflection due to bending only. In addition, we assume manipulator extension to be negligible, since displacements due to extension will be small compared with deflections caused by bending.

We propose a model that approximates manipulator shape by a serial chain of rigid links, connected by rotational joints [see Fig. 2(a)]. Choosing multiple links for a manipulator segment enables the description of nonconstant curvature bending of the manipulator segment, which occurs in the case of external loading. Each link approximates a constant-curvature arc, defined by the following arc parameters: a fixed arc-length (l_s), the bending direction (φ_i), and the bend angle (θ_i). The rotation matrix between two joints consists of three consecutive rotations, resulting in the following rotation matrix:

$$\boldsymbol{R}^i_{i+1} = \boldsymbol{R}_z(q_{\varphi,i})\boldsymbol{R}_y(q_{\theta,i})\boldsymbol{R}_z(-q_{\varphi,i}) \in \mathrm{SO}(3) \quad (1)$$

where $\boldsymbol{R}_z, \boldsymbol{R}_y \in \mathrm{SO}(3)$ are rotations about the z-axis and y-axis of the rotated frame, respectively. Link rotation in (1) is given by two angles: The first angle ($q_{\varphi,i}$) indicates the bending direction, and the second angle ($q_{\theta,i}$) is related to the amount of bending [see Fig. 2(b)]. Given the position ($\boldsymbol{p}^i_{i+1}$) of the current joint with respect to the previous joint, the transformation matrix is given as

$$\boldsymbol{H}^i_{i+1} = \begin{bmatrix} \boldsymbol{R}^i_{i+1} & \boldsymbol{p}^i_{i+1} \\ \boldsymbol{0}^3 & 1 \end{bmatrix} \in \mathrm{SE}(3). \quad (2)$$

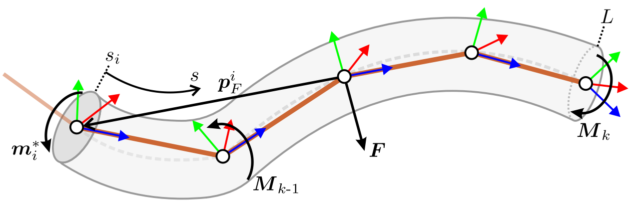

Fig. 3. Bending moment ($\boldsymbol{m}_i^*$), at the location of the ith joint, is the sum of moments due to actuation ($\boldsymbol{M}_j$), and moments due to external loads ($\boldsymbol{F}$) acting on the manipulator.

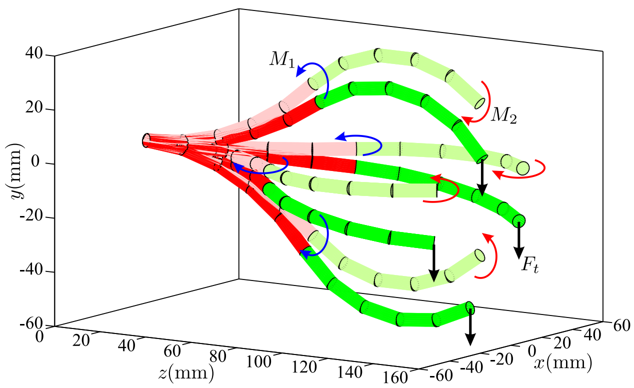

Fig. 4. Rigid-link modeling of a manipulator with two segments (red and green), approximated by ten rigid links. Moments are applied midway (M_1) the manipulator and at the tip (M_2) in different directions, resulting in four different configurations. Two cases are shown for each configuration: Unloaded case without external forces (light colored), and a loaded case (dark colored) with an external force (F_t) at the tip in the negative y-direction.

The forward kinematics of a continuum manipulator, approximated by n rigid links, is calculated by postmultiplying the individual transformations of each link.

In order to account for manipulator stiffness, rotational springs (K_θ) are assigned at the origin and at the end of each link [see Fig. 2(b)]. Due to the approximation of a constant-curvature arc by a rigid link, the energy ($U_{s,i}$) stored in the springs can be described in terms of the bend angle (θ_i) as

$$U_{s,i} = \frac{1}{2}K_\theta\left(\frac{\theta_i}{2}\right)^2 + \frac{1}{2}K_\theta\left(\frac{\theta_i}{2}\right)^2 = \frac{1}{4}K_\theta{\theta_i}^2. \tag{3}$$

The spring energy approximates the strain energy due to manipulator bending. The strain energy ($U_{b,i}$) of a constant-curvature arc, with fixed length (l_s), is given by [20]

$$U_{b,i} = \frac{1}{2}\frac{EI}{l_s}{\theta_i}^2 \tag{4}$$

where E and I are the Young's modulus and the area moment of inertia of the manipulator, respectively. Since the spring energy (3) should equal the strain energy due to bending (4), the following expression for the joint stiffness is found:

$$K_\theta = \frac{2EI}{l_s}. \tag{5}$$

We assume the Young's modulus (E) and the area moment of inertia (I) to be constant along the length of the manipulator such that the stiffness (K_θ) for each joint is equal. For a joint located between two rigid links, two rotational springs are connected in series such that the equivalent joint stiffness (K_r) is given as

$$K_r = \left(\frac{1}{K_\theta} + \frac{1}{K_\theta}\right)^{-1} = \frac{EI}{l_s}. \tag{6}$$

Given this stiffness, the torque at the ith joint can be written as

$$\tau_i = K_r q_{\theta,i} \tag{7}$$

where $q_{\theta,i}$ is the joint angle related to the amount of bending. In the next section, we relate both joint angles ($q_{\varphi,i}$ and $q_{\theta,i}$) of the rigid-link model to the internal bending moment of the manipulator, which is used to calculate manipulator shape.

B. Shape Calculation

In the previous section, we presented a model that describes manipulator shape by a serial chain of rigid links, connected by flexible rotational joints. In order to determine manipulator shape, the individual joint angles need to be calculated. The internal bending moment ($\boldsymbol{m}(s)$) of the manipulator defines the direction and the amount of bending. In the case of the rigid-link model, we relate the internal bending moment at the location of the ith joint ($\boldsymbol{m}_i^*$) to the joint angles by

$$\begin{aligned} K_r q_{\theta,i} &= \| \boldsymbol{m}_i^* \| \\ q_{\varphi,i} &= \angle \boldsymbol{m}_i^* \end{aligned} \tag{8}$$

such that $q_{\theta,i}$ and $q_{\varphi,i}$ are related to the magnitude and the direction of the bending moment, respectively. The magnitude of the internal bending moment ($\boldsymbol{m}_i^*$) is equal to the joint torque as given by (7). Considering concentrated loads only, the bending moment at the ith joint is determined by the forces and moments that act on the remaining part (i.e., $s = s_i \ldots L$) of the manipulator shaft (see Fig. 3):

$$\boldsymbol{m}_i^* = \sum \boldsymbol{M}_j + \boldsymbol{p}_F^i \times \boldsymbol{F} \tag{9}$$

where $\boldsymbol{M}_j$ is the moment resulting from actuation, and $\boldsymbol{F}$ denotes an external force. The position vector ($\boldsymbol{p}_F^i$) in (9) depends on the final manipulator configuration and can be expressed in terms of the joint angles using the rigid-link kinematics. Substituting (9) into (8) for each joint results in a set of nonlinear equations from which the joint angles need to be solved in order to calculate manipulator shape.

In order to demonstrate the modeling approach, as an example, we calculate the shape of a continuum manipulator with two bending segments under different loading conditions. The manipulator is approximated by ten rigid links, and actuation moments are applied midway ($M_1 = -150$ N $\cdot$ mm) the manipulator and at the tip ($M_2 = 100$ N $\cdot$ mm). Manipulator properties are provided in Table I in Section V. The direction of the moments is varied, resulting in four different manipulator configurations (see Fig. 4). For each configuration, we calculate the shape for the unloaded case and for the loaded case with an external force ($F_t = -0.1$ N) at the tip. The model is evaluated using MATLAB, and the function `fsolve` is used to solve the joint angles from the set of nonlinear equations. In Section VI, we compare deflection calculated using our rigid-link model with the Cosserat rod model.

C. Jacobian Calculation

In this section, we show the derivation of the manipulator Jacobian of the rigid-link model, which will be used for control. The manipulator Jacobian ($\boldsymbol{J}(\boldsymbol{q})$) relates joint velocities ($\dot{\boldsymbol{q}}$) to end-effector velocity ($\boldsymbol{v}_e \in \mathbb{R}^6$)

$$\boldsymbol{v}_e = \begin{bmatrix} \boldsymbol{\omega}_e \\ \dot{\boldsymbol{p}}_e \end{bmatrix} = \boldsymbol{J}(\boldsymbol{q})\dot{\boldsymbol{q}} \tag{10}$$

where $\boldsymbol{\omega}_e \in \mathbb{R}^3$ and $\dot{\boldsymbol{p}}_e \in \mathbb{R}^3$ are the end-effector angular velocity and linear velocity, respectively. For a manipulator approximated by a serial chain of n rigid links, there are a total of $2 \times n$ joints since each link (i) is described by two joint angles: the direction of bending ($q_{\varphi,i}$) and the bending angle ($q_{\theta,i}$). Thus, (10) can be rewritten as

$$\boldsymbol{v}_e = \boldsymbol{J}_1(\boldsymbol{q}) \begin{bmatrix} \dot{q}_{\varphi,1} \\ \dot{q}_{\theta,1} \end{bmatrix} + \boldsymbol{J}_2(\boldsymbol{q}) \begin{bmatrix} \dot{q}_{\varphi,2} \\ \dot{q}_{\theta,2} \end{bmatrix} + \cdots \boldsymbol{J}_n(\boldsymbol{q}) \begin{bmatrix} \dot{q}_{\varphi,n} \\ \dot{q}_{\theta,n} \end{bmatrix} \tag{11}$$

where $\boldsymbol{J}_i(\boldsymbol{q}) \in \mathbb{R}^{6\times 2}$ is the Jacobian for a single link of the manipulator and can be written as

$$\boldsymbol{J}_i(\boldsymbol{q}) = \begin{bmatrix} \boldsymbol{\xi}'_\varphi & \boldsymbol{\xi}'_\theta \end{bmatrix} \tag{12}$$

where $\boldsymbol{\xi}'_\varphi \in \mathbb{R}^6$ and $\boldsymbol{\xi}'_\theta \in \mathbb{R}^6$ are the twist coordinates of the joint twists related to the direction of bending and the bending angle, respectively [21]. The twists in (12) are calculated by transforming the unit joint twists ($\boldsymbol{\xi}_j$) to the current manipulator configuration

$$\boldsymbol{\xi}'_j = \mathrm{Ad}_{\boldsymbol{H}^0_{j-1}} \boldsymbol{\xi}_j \tag{13}$$

where $\mathrm{Ad}_{\boldsymbol{H}^0_{j-1}} \in \mathbb{R}^{6\times 6}$ is the adjoint matrix, which depends on manipulator configuration [21]. Since all joints are revolute, the unit twist of each joint with respect to the previous joint is given as

$$\boldsymbol{\xi}_j = \begin{pmatrix} \hat{\boldsymbol{\omega}} \\ \boldsymbol{r} \times \hat{\boldsymbol{\omega}} \end{pmatrix} \tag{14}$$

where $\hat{\boldsymbol{\omega}} \in \mathbb{R}^3$ denotes the unit angular velocity, and $\boldsymbol{r} \in \mathbb{R}^3$ is the position vector from the origin of the previous joint to the origin of the current joint. In the next section, we propose a controller based on the manipulator Jacobian of the rigid-link model.

III. Steering of a Tendon-Driven Continuum Manipulator

In this section, we present a method for the steering of a tendon-driven continuum manipulator based on the rigid-link model. First, a kinematic controller is presented, which calculates the joint angles related to the rigid-link model. From the joint angles, the actuation moments that need to be applied at the end of each segment are calculated. Finally, we discuss a manipulator-specific model that computes tendon lengths from the actuation moments.

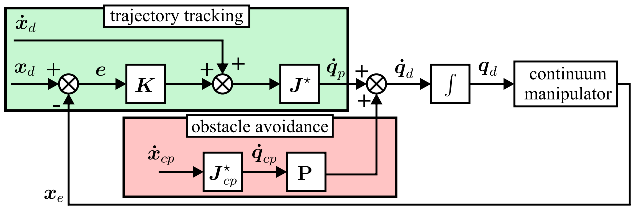

Fig. 5. Architecture of the controller: The primary task is trajectory tracking of the manipulator tip. The secondary task consists of avoiding obstacles with the manipulator shaft.

A. Kinematic Control

In order to steer the manipulator tip to a desired location, the IK of the manipulator needs to be solved. Finding a closed-form solution for the IK problem for a continuum manipulator with multiple segments is not straightforward. However, the IK problem can be solved by using the manipulator Jacobian ($\boldsymbol{J}$) that was derived in Section II-C. A well-known method for solving the IK problem is the damped least squares (DLS) inverse [22]

$$\dot{\boldsymbol{q}}_{\boldsymbol{d}} = \boldsymbol{J}^\star \dot{\boldsymbol{x}}_d \tag{15}$$

where $\dot{\boldsymbol{x}}_d \in \mathbb{R}^6$ is the desired manipulator tip velocity in the task space, and $\boldsymbol{J}^\star$ is the DLS inverse of the manipulator Jacobian. The joint positions ($\boldsymbol{q}_d$) can be calculated by integrating the joint velocities ($\dot{\boldsymbol{q}}_{\boldsymbol{d}}$) over time.

We define a primary task that consists of steering the manipulator tip along a reference trajectory, for which we propose the following kinematic controller:

$$\dot{\boldsymbol{q}}_{\boldsymbol{d}} = \boldsymbol{J}^\star \left(\dot{\boldsymbol{x}}_d + \boldsymbol{K}\boldsymbol{e}\right) \tag{16}$$

where $\boldsymbol{K}$ is a gain matrix, and $\boldsymbol{e}$ is the trajectory tracking error. Continuum manipulators with multiple segments often have more degrees of freedom (DOF) than required for the intended task, which means the manipulator is kinematically redundant and this allows us to rewrite (16) as [22]

$$\dot{\boldsymbol{q}}_{\boldsymbol{d}} = \boldsymbol{J}^\star \left(\dot{\boldsymbol{x}}_d + \boldsymbol{K}\boldsymbol{e}\right) + \boldsymbol{P}\dot{\boldsymbol{q}}_0 \tag{17}$$

where $\boldsymbol{P}$ is a matrix given by

$$\boldsymbol{P} = \left(\boldsymbol{I} - \boldsymbol{J}^\star \boldsymbol{J}\right) \tag{18}$$

and projects a vector of arbitrary joint velocities ($\dot{\boldsymbol{q}}_0$) into the null space of the manipulator Jacobian. Joint velocities in the null space do not cause motion of the manipulator tip; hence, this can be used to define a secondary task of obstacle avoidance along with the primary task of trajectory tracking.

In order to avoid obstacles, a motion ($\dot{\boldsymbol{x}}_{\mathrm{cp}} \in \mathbb{R}^3$) is defined for the point (critical point) on the manipulator that is closest to the obstacle. Given the position of the critical point on the manipulator, the Jacobian ($\boldsymbol{J}_{\mathrm{cp}}$) that relates joint velocities to the velocity of the critical point can be calculated. Using this critical-point Jacobian, the joint velocities that result in the desired motion of the critical point can be calculated by

$$\dot{\boldsymbol{q}}_{\mathrm{cp}} = \boldsymbol{J}^\star_{\mathrm{cp}} \dot{\boldsymbol{x}}_{\mathrm{cp}} \tag{19}$$

where $\boldsymbol{J}^\star_{\mathrm{cp}}$ is the DLS inverse of the critical-point Jacobian. Substituting this into (17) for the null space joint velocities ($\dot{\boldsymbol{q}}_0$)

gives the following solution of the IK with obstacle avoidance (see Fig. 5):

$$\dot{\boldsymbol{q}}_{\boldsymbol{d}} = \boldsymbol{J}^{\star}\left(\dot{\boldsymbol{x}}_d + \boldsymbol{K}\boldsymbol{e}\right) + \boldsymbol{P}\boldsymbol{J}^{\star}_{\mathrm{cp}}\dot{\boldsymbol{x}}_{\mathrm{cp}}. \tag{20}$$

The actuation moments that result in the desired joint angles need to be calculated. Assuming quasi-static motion, we use the following well-known relationship that uses the transpose of the manipulator Jacobian ($\boldsymbol{J}$) to relate a wrench acting on the manipulator tip to the joint torques in static equilibrium [22]:

$$\boldsymbol{\tau} = \boldsymbol{J}^T \boldsymbol{f}_t \tag{21}$$

where $\boldsymbol{\tau}$ is the vector containing the joint torques, and $\boldsymbol{f}_t \in \mathbb{R}^6$ is the wrench applied at the manipulator tip, given by

$$\boldsymbol{f}_t = \begin{bmatrix} \boldsymbol{M}_t & \boldsymbol{F}_t \end{bmatrix}^T \tag{22}$$

where $\boldsymbol{M}_t \in \mathbb{R}^3$ and $\boldsymbol{F}_t \in \mathbb{R}^3$ are the tip moment and tip force, respectively. In the case of a manipulator with k segments, a wrench ($\boldsymbol{f}_i$) is applied at the end of each segment; hence, the joint torques (τ_i) are given by

$$\begin{bmatrix} \tau_1 \\ \tau_2 \\ \vdots \\ \tau_k \end{bmatrix} = \begin{bmatrix} \boldsymbol{J}_1^T & \boldsymbol{J}_2^T & \cdots & \boldsymbol{J}_k^T \\ & \boldsymbol{J}_2^T & \cdots & \vdots \\ & & \ddots & \vdots \\ \boldsymbol{0} & & & \boldsymbol{J}_k^T \end{bmatrix} \begin{bmatrix} \boldsymbol{f}_1 \\ \boldsymbol{f}_2 \\ \vdots \\ \boldsymbol{f}_k \end{bmatrix} \tag{23}$$

where $\boldsymbol{J}_i$ is the Jacobian for the ith manipulator segment. Rewriting (23) gives

$$\boldsymbol{\tau} = \boldsymbol{\Upsilon}\boldsymbol{F} \tag{24}$$

where $\boldsymbol{\Upsilon}$ is a matrix containing the transpose of the Jacobian of each segment (23), and $\boldsymbol{F} = [\boldsymbol{f}_1 \ \ldots \ \boldsymbol{f}_k]$ is the vector with wrenches ($\boldsymbol{f}_i$) applied at the end of each segment. The joint torques can be calculated by multiplying the joint angles ($q_{\theta,i}$) that are related to the amount of bending with the corresponding joint stiffness, as given by (7). The actuation moment that needs to be generated at the end of each segment can then be calculated by

$$\boldsymbol{F} = \boldsymbol{\Upsilon}^{-1}\boldsymbol{\tau}. \tag{25}$$

In the next section, we describe a manipulator-specific model, which calculates tendon lengths from the actuation moments.

B. Manipulator-Specific Model

Actuation moments in tendon-driven continuum manipulators are generated by tendons that are fixed at the end of each segment (see Fig. 6). Pulling on the tendons generates a moment, and this results in constant-curvature bending of the segment. Hence, each segment can be described by two arc parameters: the bending angle (θ_i) and bending direction (φ_i). In the case of multiple segments, tendon loads and tendon paths between segments are coupled. The model relates changes in tendon lengths to the bending moment along the segments. As opposed to the model presented by Camarillo *et al.*, in the derivation below, we do not consider axial shortening of the manipulator since we consider the manipulator to be inextensible [23].

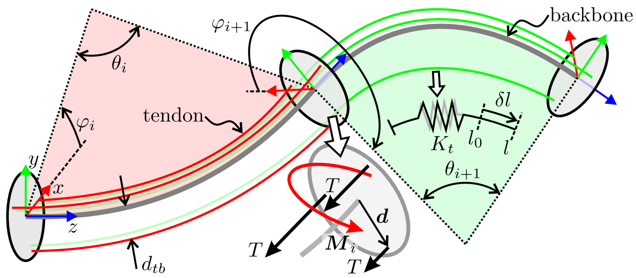

Fig. 6. Model of a multisegment tendon-driven continuum manipulator: Due to tendon tension (T) at a distance (d_{tb}) from the backbone, a moment ($\boldsymbol{M}_i$) is generated at the end of the segment where the tendons are fixed. This moment results in constant-curvature bending of the segment such that each segment can be described by two arc parameters: The bending angle (θ_i) and the bending direction (φ_i). Each tendon is modeled as a linear elastic spring (K_t), such that the change in tendon length (δl) depends both on manipulator shape and tendon elongation.

At this stage of our derivation, we neglect the friction between the tendons and tendon guides. Therefore, upon actuation, the tension (T) in the tendon causes a moment ($\boldsymbol{M}_t$) equal to

$$\boldsymbol{M}_t = \begin{bmatrix} d_x \\ d_y \\ 0 \end{bmatrix} \times \begin{bmatrix} 0 \\ 0 \\ T \end{bmatrix} = \begin{bmatrix} d_y T \\ -d_x T \\ 0 \end{bmatrix} \tag{26}$$

where d_x and d_y denote the x-position and y-position of the tendon in the cross section of the manipulator (see Fig. 6) and define the moment arm for the tendon. For a total of p tendons for each segment, the total moment ($\boldsymbol{M}_i$) generated at the end of the ith segment is the sum of the individual moments

$$\boldsymbol{M}_i = \sum_{k=1}^{p} \boldsymbol{M}_{t,k} = \underbrace{\begin{bmatrix} d_{y,1} & d_{y,2} & \cdots & d_{y,p} \\ -d_{x,1} & -d_{x,2} & \cdots & -d_{x,p} \end{bmatrix}}_{\boldsymbol{D}_i} \begin{bmatrix} T_1 \\ \vdots \\ T_p \end{bmatrix} \tag{27}$$

where $\boldsymbol{D}_i$ is a matrix that contains the tendon moment arms. For a manipulator with k segments, the bending moment along the ith segment ($\boldsymbol{m}_i$) is calculated by summing the moments generated at the end of distal segments

$$\boldsymbol{m}_i = \sum_{j=i}^{k} \boldsymbol{M}_j = \sum_{j=i}^{k} \boldsymbol{D}_j \boldsymbol{T}_j \tag{28}$$

where $\boldsymbol{T}_j \in \mathbb{R}^p$ is the tendon tension vector for the jth segment. Expanding (28) for all segments gives

$$\begin{bmatrix} \boldsymbol{m}_1 \\ \boldsymbol{m}_2 \\ \vdots \\ \boldsymbol{m}_k \end{bmatrix} = \begin{bmatrix} \boldsymbol{D}_1 & \boldsymbol{D}_2 & \cdots & \boldsymbol{D}_k \\ & \boldsymbol{D}_2 & \cdots & \vdots \\ & & \ddots & \vdots \\ \boldsymbol{0} & & & \boldsymbol{D}_k \end{bmatrix} \begin{bmatrix} \boldsymbol{T}_1 \\ \boldsymbol{T}_2 \\ \vdots \\ \boldsymbol{T}_k \end{bmatrix}. \tag{29}$$

Assuming position control, in which tendon length is controlled, the relation between tendon tension and change in tendon length needs to be found. The change in tendon length can be written as

$$\delta l = \delta l_b + \delta l_t \tag{30}$$

where δl_b and δl_t are the changes in tendon length due to manipulator bending and tendon elongation, respectively. The change in tendon length due to bending is given by

$$\delta l_b = l_0 \varepsilon_b = l_0 \left(\varepsilon_{b,x} + \varepsilon_{b,y}\right) = l_0 \left(d_y \kappa_x - d_x \kappa_y\right) \tag{31}$$

where l_0 is the tendon length in the reference configuration, and $\varepsilon_{b,x}$ and $\varepsilon_{b,y}$ are the strains along the tendon path due to bending about the x-axis and the y-axis, respectively. Tension in the tendon results in elongation of the tendon by

$$\delta l_t = \frac{1}{K_t} T \tag{32}$$

where K_t is the tendon stiffness. Rewriting (31) and (32) for all tendons in the manipulator and substituting into (30) gives the following expression for the change in tendon lengths:

$$\delta \boldsymbol{l} = l_0 \boldsymbol{D}^T \boldsymbol{\kappa} + \boldsymbol{K}_t^{-1} \boldsymbol{T} \tag{33}$$

where $\boldsymbol{D}$ is the matrix with the tendon moment arms for all segments given in (29), and $\boldsymbol{K}_t \in \mathbb{R}^{pk \times pk}$ is a diagonal matrix with the stiffness of the individual tendons on the diagonal. The curvature vector ($\boldsymbol{\kappa}$) can be written as a function of the bending moment ($\boldsymbol{m}_i$) as

$$\boldsymbol{\kappa} = \begin{bmatrix} \kappa_x \\ \kappa_y \end{bmatrix} = \begin{bmatrix} \frac{1}{EI} & 0 \\ 0 & \frac{1}{EI} \end{bmatrix} \begin{bmatrix} m_x \\ m_y \end{bmatrix} \tag{34}$$

where m_x and m_y denote the components of the bending moment about the x-axis and y-axis, respectively. Combining (34) with (28) relates the curvature to the tendon tension by

$$\boldsymbol{\kappa} = \boldsymbol{K}_m^{-1} \boldsymbol{m}_i = \boldsymbol{K}_m^{-1} \boldsymbol{D}_i \boldsymbol{T}_i \tag{35}$$

where $\boldsymbol{K}_m$ is a diagonal matrix with the flexural rigidity (EI) for each segment of the manipulator on the diagonal. Substituting (35) for the curvature into (33) allows us to write the change in tendon lengths as

$$\delta \boldsymbol{l} = \left(l_0 \boldsymbol{D}^T \boldsymbol{K}_m^{-1} \boldsymbol{D} + \boldsymbol{K}_t^{-1}\right) \boldsymbol{T} = \boldsymbol{C}_m \boldsymbol{T} \tag{36}$$

where $\boldsymbol{C}_m$ is the compliance matrix. The compliance matrix allows us to calculate changes in tendon lengths from tendon tensions.

In the next section, we describe 3-D reconstruction of manipulator shape using FBG sensors. Closed-loop control is achieved by feedback of manipulator shape in the controller presented in this section.

IV. Shape Reconstruction Using Fiber Bragg Grating Sensors

In order to perform closed-loop control, information about the position and orientation of the instrument is required. Different medical imaging modalities exist that can give information about instrument pose, e.g., computed tomography (CT), ultrasound (US) imaging, and magnetic resonance imaging (MRI). However, these modalities are often slow (i.e., CT and MRI) or they suffer from a low resolution (US). In addition, additional

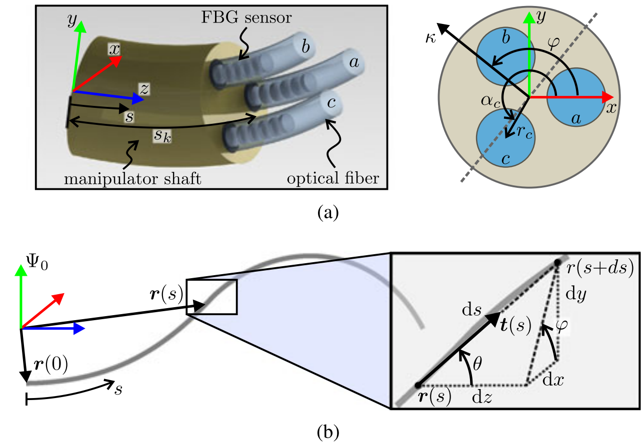

Fig. 7. (a) Three colocated FBG sensors, placed in separate optical fibers (a, b, and c), measure axial strain at different locations along the shaft. Manipulator curvature (κ) and its direction (φ) are determined from the measured strains. (b) Manipulator is represented as a spatial curve ($\boldsymbol{r}(s)$), of which the shape is reconstructed by integrating the tangent vector ($\boldsymbol{t}(s)$). The orientation of the tangent vector is given by two angles, the bending angle (θ) and the bending direction (φ), which are both computed from the FBG strain measurements.

image processing techniques are required in order to determine 3-D instrument shape from one or multiple images. A method for shape sensing of continuum manipulators, which does not rely on imaging, is presented by Trivedi and Rahn [24]. However, their methods are based on a geometrically exact model and require knowledge about manipulator properties.

FBGs offer the possibility to determine the 3-D shape of a flexible instrument. Due to the small diameter of optical fibers ($\leq 250\,\mu$m), they can easily be integrated in small-diameter instruments. Current technology enables to read these strains at rates up to 20 kHz, which is much faster than existing imaging modalities. FBGs can be seen as optical strain gauges and can be used as sensors to measure strain [25]. In previous studies, we have investigated shape sensing using FBG sensors for needle steering applications and for the control of a manipulator in free space [19], [26]. In both cases, strain was measured from sets of three colocated FBG sensors in optical fibers (a, b, and c) that were placed along the length of the manipulator [see Fig. 7(a)]. The strain measured by each sensor, at a location (s_k) along the shaft, is given by [26]

$$\varepsilon_*(s_k) = \kappa(s_k) r_* \sin(\varphi(s_k) + \alpha_*) + \varepsilon_0(s_k) \tag{37}$$

where r_* and α_* denote the position and orientation of the fiber center (for $* = a, b, c$) at the cross section, respectively. The curvature ($\kappa(s_k)$) and its direction ($\varphi(s_k)$) are computed from the set of measured strains (37). Interpolation of the discrete curvatures ($\kappa(s_k)$) and their corresponding directions ($\varphi(s_k)$) is performed in order to approximate them (i.e., $\kappa(s)$ and $\varphi(s)$) along the length of the manipulator [26].

We consider the manipulator as a spatial curve, parameterized by the arc length (s) and defined by the position vector ($\boldsymbol{r}(s)$). The tangent vector along the curve is defined as the derivative of the position vector with respect to the arc length [see Fig. 7(b)]

$$\boldsymbol{t}(s) = \frac{d\boldsymbol{r}(s)}{ds} = \begin{bmatrix} \frac{dx}{ds} & \frac{dy}{ds} & \frac{dz}{ds} \end{bmatrix}^T. \tag{38}$$

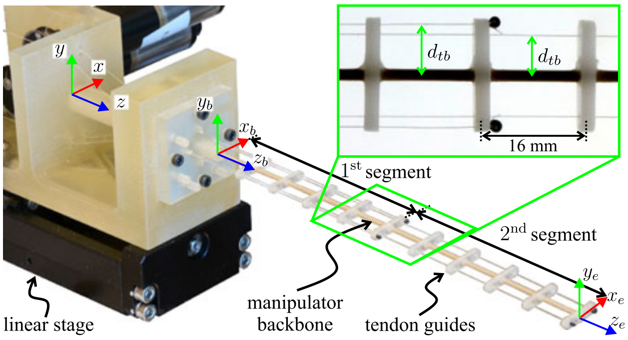

Fig. 8. Experimental setup consisting of a planar tendon-driven continuum manipulator with two segments, each with a length of 80 mm. Tendon guides are glued along the manipulator backbone with a spacing of 16 mm. Each segment is actuated by a pair of opposing tendons. Tendon offset (d_{tb}) from the backbone is 7.5 and 6.0 mm for the first and second segment, respectively. The manipulator is mounted on a linear stage to allow translation in the insertion direction (i.e., z-direction).

The orientation of the tangent vector, with respect to the global reference frame (Ψ_0), is given by two angles [see Fig. 7(b)]. The first angle is the bending angle (θ) and is defined as the angle between the tangent vector and the z-axis. The second angle equals the bending direction (φ) of the manipulator and is given by the orientation of the tangent vector in the xy-plane, with respect to the x-axis. The bending direction is directly measured by the FBG sensors, while integration of the curvature ($\kappa(s)$) is required to compute the bending angle ($\theta(s)$) along the manipulator shaft

$$\theta(s) = \int \kappa(s) ds + \theta_0 \tag{39}$$

where θ_0 is the initial angle. Using goniometry, the tangent vector can be expressed in terms of the bending angle and bending direction. Manipulator shape is then reconstructed by integrating the tangent vector

$$\boldsymbol{r}(s) = \int \boldsymbol{t}(s) ds + \boldsymbol{r}(0) \tag{40}$$

where $\boldsymbol{r}(0)$ is the initial position.

Each sensor measures a strain component that is independent of bending, which is denoted by ε_0 in (37). This component represents the axial strain due to compression and extension of the manipulator shaft. Hence, this can be used for measuring axial forces that act along the manipulator. In the experiments, FBG sensors are used for shape sensing in order to enable closed-loop control of the manipulator, and FBG sensors will also be investigated for force sensing. In the next section, we discuss the experimental testbed, which includes FBG-based shape sensing.

V. Experimental Testbed

The experimental testbed consists of a planar tendon-driven continuum manipulator with two segments (see Fig. 8). Each segment is actuated by a pair of opposing tendons made from Dyneema. The manipulator has a backbone made from PolyEther Ether Ketone (PEEK) tubing (diameter ϕ_{inner} 1.07 mm, ϕ_{outer} 1.8 mm) with a length of 160 mm, with each segment having a length of 80 mm. Tendon guides are laser cut from Delrin and are glued along the backbone at a spacing of 16 mm. The first tendon pair is routed through the tendon guides at an offset (d_{tb}) of 7.5 mm, and the second pair has an offset of 6.0 mm. Each tendon is actuated by a Maxon EC-max 22 motor (Maxon motor Ag, Sachseln, Switzerland). Each motor is controlled using an Elmo Whistle motor controller (Elmo Motion Control Ltd., Petach-Tikva, Israel). The continuum manipulator and motors are fixed on a 3-D printed platform, which is mounted on a linear stage to provide insertion along the z-direction of the manipulator.

TABLE I
Model Inputs for the Tendon-Driven Continuum Manipulator

Parameter		Symbol	Value
Young's modulus	Peek	E_p	3.8 GPa [27]
	Nitinol	E_n	75 GPa
Tendon offset	Segment 1	d_{tb}	7.5 mm
	Segment 2		6.0 mm
Tendon stiffness	Segment 1		5.37 N/mm
			4.15 N/mm
	Segment 2	K_t	5.12 N/mm
			3.92 N/mm

In order to provide shape sensing of the continuum manipulator, an nitinol wire (diameter ϕ 1.0 mm) with an integrated array of 12 FBG sensors is introduced into the hollow backbone of the manipulator. Three fibers with four FBG sensors each are integrated onto this nitinol wire. Further fabrication details of this wire with integrated FBG sensors are provided by Roesthuis *et al.* [19]. The fibers are connected to a Deminsys Python interrogator (Technobis Fiber Technologies, Uitgeest, The Netherlands) in order to provide communication with a desktop computer. The interrogator receives the reflected light and measures the change in reflected Bragg wavelength for each FBG sensor.

The interrogator is connected to a desktop computer via an Ethernet connection, and communication is done using the UDP protocol. Shape reconstruction and the controller are implemented in a multithreaded C++ application, from which desired motor positions are sent to the Elmo motor controllers via a CAN bus. Packets are sent at a rate of 100 Hz, and the controller operates at the same rate.

VI. Experimental Results

This section presents the experimental results with the tendon-driven manipulator described in the previous section. First, the modeling framework presented in Section II is validated. Next, the controller presented in Section III is evaluated for two different experimental cases. Finally, we perform an experiment in which we investigate the potential of using FBG sensors for measuring axial tip interaction forces.

A. Rigid-Link Model Versus Cosserat Rod

We compare the rigid-link model to the Cosserat rod model by evaluating the difference in tip position (i.e., tip error) between both models for different loading conditions. Tendon induced moments are applied midway the manipulator (M_1) and

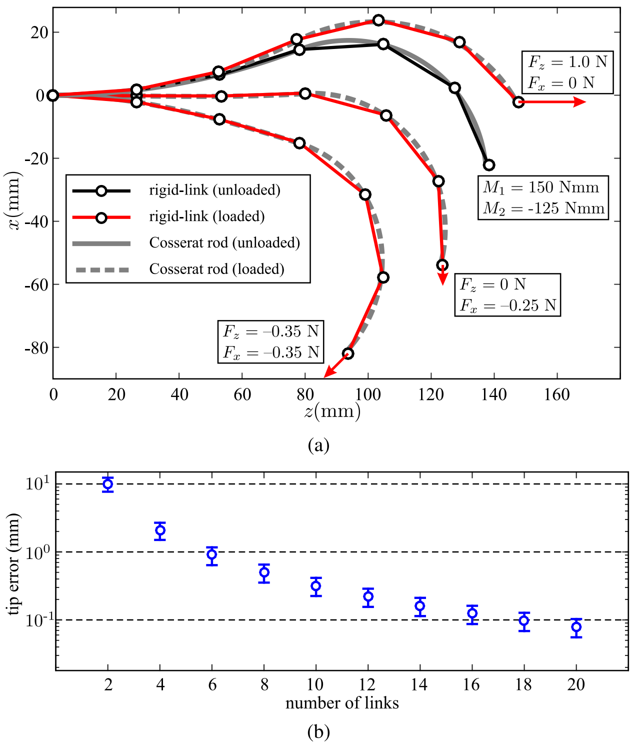

Fig. 9. (a) Rigid-link model ($n = 6$) is compared with the Cosserat rod model for different loading cases. The actuation moments midway (M_1) the manipulator and at the tip (M_2) are the same, while the magnitude and direction of the tip force is varied. (b) Difference in tip position (i.e., tip error) between the rigid-link model and the Cosserat rod model versus the amount of rigid links. The mean and the standard deviation of the tip error are shown for all cases combined.

at the tip (M_2). In order to investigate deflection under external loading, a force is applied at the manipulator tip. We follow the approach described by Rucker and Webster to calculate manipulator shape using the Cosserat rod model for a planar manipulator with two segments and a tip force [18]. Material and geometrical properties are used from the manipulator described in Section V.

Manipulator shape is computed for four different loading conditions: one unloaded case and three loaded cases in which a tip force is present [see Fig. 9(a)]. For each case, the actuation moments are equal: The moment midway the manipulator is 150 N $\cdot$ mm, while the moment at the tip is -125 N $\cdot$ mm. The mean and the standard deviation of the tip error, for all loading cases combined, are presented in Fig. 9(b). It can be seen that the tip error rapidly decreases when increasing the number of rigid links. For 20 links, the mean tip error is less than 0.1 mm. Further increasing the number of links does not increase accuracy drastically; hence, we will use 20 links for the rigid-link model in our experiments.

B. Model Validation

The manipulator-specific model from Section III-B is verified by commanding desired bending angles to the manipulator. Tendon positions are calculated from the bending angles using the manipulator-specific model, and these positions are commanded to the manipulator. The resulting manipu-

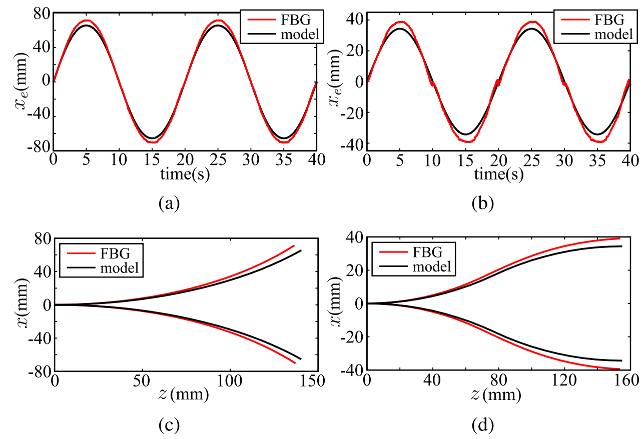

Fig. 10. Validation of the continuum manipulator model using the reconstructed shape from FBG measurements. The manipulator is deflected for the single bend case [(a) and (c)] and double bend case [(b) and (d)]. Manipulator tip deflection in the x-direction for (a) single bend and (b) double bend cases. Manipulator shape comparison for maximum and minimum deflection for (c) single bend and (d) double bend cases.

lator deflection, using the FBG sensors, is compared with the deflection obtained from the model. The inputs to the model are listed in Table I. The stiffness of each tendon is experimentally determined in a manipulator deflection experiment in which only the tendon under consideration is tensioned.

Sinusoidal bending angles are commanded to both segments of the manipulator at a frequency of 0.1 Hz with an amplitude of 25°. In the first case, the bending angles are equal and in the same direction, resulting in a single bend shape. In the second case, the bending angles are equal but of opposite direction, resulting in a double bend shape. The transverse tip deflections (x-direction) along the entire trajectory are shown in Fig. 10(a) and (b). The maximum tip error is 6.51 mm for the single bend deflection case, and 6.34 mm for the double bend deflection case. Manipulator shape at maximum bending angles (25°) is shown in Fig. 10(c) and (d). In these cases, the mean errors along the entire manipulator are calculated: Maximum errors are 2.66 mm for the single bend case and 2.15 mm for the double bend case. These errors may be caused by friction between tendons and tendon guides, which was not accounted for in the model.

C. Trajectory Tracking Experiments With Obstacle Avoidance

Experiments are performed in which the manipulator tip is commanded to track a reference trajectory, while the manipulator shaft avoids obstacles (see Fig. 11). Our manipulator has three DOFs: translation of the manipulator base (q_1) and the bend angles (q_2 and q_3) of the two segments. Since we control the position of the manipulator tip in a plane, the task is two DOFs, and we have kinematic redundancy. We derive the manipulator Jacobian ($\boldsymbol{J}(\boldsymbol{q})$) using the methods described in Section II-C. Three types of control schemes are evaluated: First, steering is performed in open loop. Second, steering is performed in closed loop according to the scheme in Fig. 5. Finally, the manipulator is steered in closed loop without avoiding

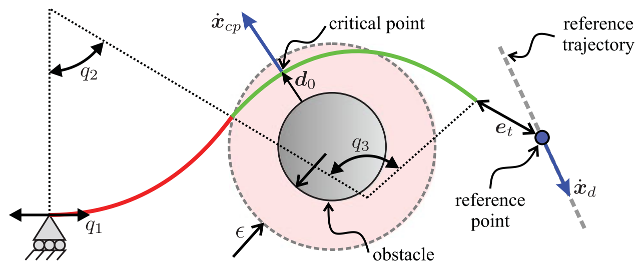

Fig. 11. Manipulator tip is controlled to track a reference trajectory, while the manipulator shaft avoids obstacles. A motion ($\dot{\boldsymbol{x}}_{\rm cp}$) is defined for the point closest to the obstacle when the manipulator is within the neighborhood of the obstacle (i.e., $\| \boldsymbol{d}_0 \| \leq \epsilon$). Trajectory tracking error is denoted by $\boldsymbol{e}_t$. The manipulator has three DOFs: translation of the base (q_1) and bending of the two segments (q_2 and q_3).

obstacles (noa). Unit gains are chosen for the gain matrix ($\boldsymbol{K}$) in (20). In order to avoid obstacles, the following velocity is defined for the critical point [28]:

$$\dot{\boldsymbol{x}}_{\rm cp} = \begin{cases} -\dfrac{v_m}{\epsilon}\boldsymbol{d}_0 + v_m \dfrac{\boldsymbol{d}_0}{\| \boldsymbol{d}_0 \|}, & \| \boldsymbol{d}_0 \| \leq \epsilon \\ 0, & \| \boldsymbol{d}_0 \| > \epsilon \end{cases} \quad (41)$$

where $\boldsymbol{d}_0$ connects the points on the obstacle and manipulator that are closest to each other, and ϵ is the threshold distance for obstacle avoidance. The maximum velocity (v_m) for the critical point is set to 500 mm/s, and the threshold distance is set to 5 mm. The velocity ($\dot{\boldsymbol{x}}_d$) of the reference point that defines the desired trajectory is set to 5 mm/s.

The controller is demonstrated in two different scenarios: steering along a reference trajectory around a static obstacle (Case I) and steering along a reference trajectory with a moving obstacle (Case II). The results of Case I and Case II are presented in Figs. 12 and 13, respectively. The mean and maximum (absolute) tracking errors are reported in Table II. Note that the coordinates $(\cdot, \cdot)$ presented are expressed in the manipulator base frame in the initial configuration as (x, z). In both experimental cases, the manipulator tip is initially located at $(0, 160)$ mm. For Case I [see Fig. 12(a)], the manipulator tip is commanded to follow a reference trajectory around a static obstacle (ϕ 70 mm). For Case II [see Fig. 13(a)], the manipulator tip is commanded to follow a straight reference trajectory, while an obstacle (ϕ 40 mm) is moving toward the manipulator. As expected, open-loop control results in trajectory tracking errors and also a steady-state error is present [see Figs. 12(a), (c) and Figs. 13(b), (c) and also Table II]. These errors can be explained by friction between tendons and tendon guides. Near-zero trajectory tracking errors are observed for both cases of closed-loop control: The small errors can be attributed to noise in the measurements of the FBG sensors. For both open-loop and closed-loop control with obstacle avoidance, the manipulator successfully avoids the obstacle [see Figs. 12(d) and 13(d)]. The minimum distance between obstacle and manipulator is 1.4 mm for Case I and Case II is 1.1 mm. For closed-loop control without obstacle avoidance (noa), we observe that the manipulator collides with the obstacle. When approaching the obstacle (i.e., $\| \boldsymbol{d}_0 \| < \epsilon$), the bending angles of both segments are adjusted such that the critical point moves in a direction away from the obstacle [see Figs. 12(e) and 13(e)].

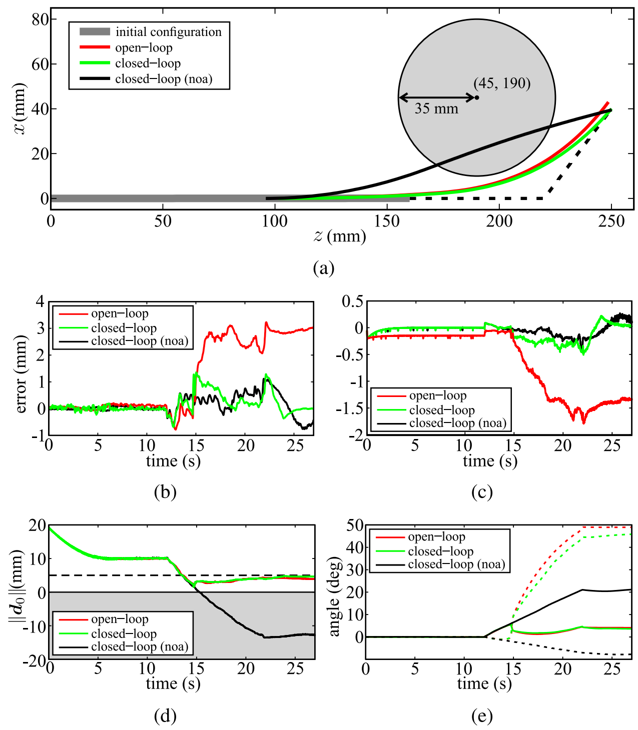

Fig. 12. Case I results. (a) Manipulator is steered along a reference trajectory (dashed) around a static obstacle (circle). Three different types of control are evaluated: open-loop (red), closed-loop (green), and closed-loop (black) without obstacle avoidance (noa). Final manipulator configuration for the three types of control is shown. (b) Tracking error in x-direction. (c) Tracking error in z-direction. (d) Distance between obstacle and manipulator ($\| \boldsymbol{d}_0 \|$). The gray area indicates collision with the obstacle, while the dashed line indicates the boundary (i.e., $\epsilon = 5$ mm) for obstacle avoidance. (e) Bending angles for both segments: q_2 (solid) and q_3 (dashed). *The accompanying video demonstrates the results of these trajectory tracking experiments.*

TABLE II
ABSOLUTE ($\| \boldsymbol{e}_t \|$) TRAJECTORY TRACKING ERRORS (IN MM) FOR BOTH EXPERIMENTAL CASES (I AND II) USING THREE TYPES OF CONTROL: OPEN-LOOP (OL), CLOSED-LOOP (CL), AND CLOSED-LOOP WITHOUT OBSTACLE AVOIDANCE (CL-NOA)

Type	Case I (mm)		Case II (mm)	
	Mean	Max	Mean	Max
OL	1.64 (0.08)	3.69 (0.03)	0.35 (0.08)	0.80 (0.07)
CL	0.24 (0.01)	1.37 (0.05)	0.09 (0.02)	0.52 (0.04)
CL-noa	0.28 (0.02)	1.35 (0.10)	0.06 (0.03)	0.38 (0.09)

The mean errors (along the entire trajectory) and maximum (max) errors are presented. Reported values are average values and standard deviations (in brackets). Each experimental case is repeated five times.

D. Feasibility of Force Sensing Using Fiber Bragg Grating Sensors

Three colocated FBG sensors can measure axial strain induced by an (axial) force besides measuring bending induced strain as shown by (37). We demonstrate this in an experiment in which the manipulator tip interacts with a compliant

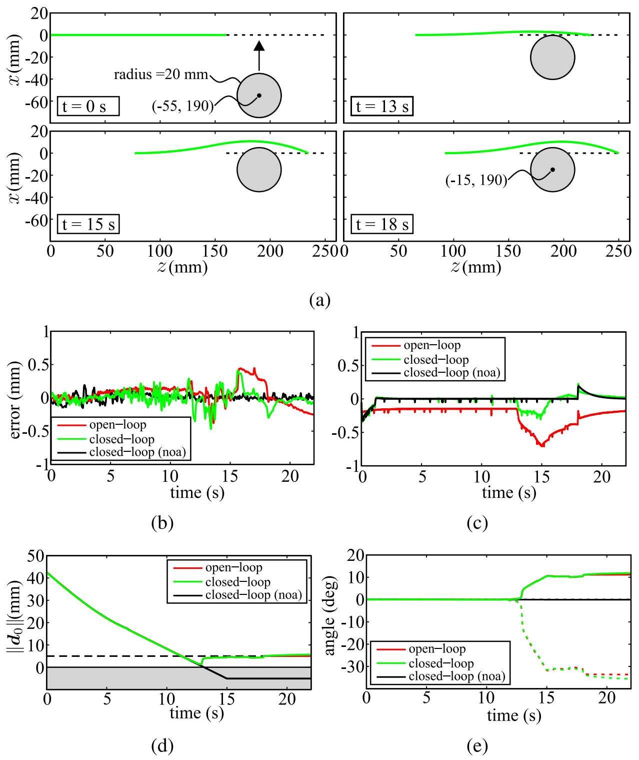

Fig. 13. Case II results. (a) Manipulator tip is steered along a reference trajectory (dashed) while avoiding a moving obstacle (circle). Three different types of control are evaluated: open-loop (red), closed-loop (green), and closed-loop (black) without obstacle avoidance (noa). Manipulator configuration (green) is shown, for the case of closed-loop control with obstacle avoidance, at different time instants during the experiment: t = 0, 13, 15 and 18 s. (b) Tracking error in x-direction. (c) Tracking error in z-direction. (d) Distance between obstacle and manipulator ($\| \boldsymbol{d}_0 \|$). The gray area indicates collision with the obstacle, while the dashed line indicates the boundary (i.e., $\epsilon = 5$ mm) for obstacle avoidance. (e) The bending angles for both segments: q_2 (solid) and q_3 (dashed). *The accompanying video demonstrates the results of these trajectory tracking experiments.*

environment. The compliant environment consists of a spring which is mounted onto an ATI Mini40 FT-sensor (ATI Industrial Automation, Apex, NC, USA).

Two experimental scenarios are considered. In the first scenario, the manipulator tip indents the compliant environment during a forward motion (i.e., no bending of manipulator). For the second scenario, the manipulator is steered in closed-loop control along a reference trajectory toward the environment. The axial strain measured by the FBG sensor near the manipulator tip is compared with the force measured by the force sensor in the insertion direction (i.e., z-direction) in Fig. 14. For the first scenario, the tip starts to interact with the environment at 6 s and further indents it until 14 s with a constant velocity of 0.5 mm/s [see Fig. 14(a)]. The strains measured by the FBG sensor follows a trend similar to the reference force. In the second scenario, the manipulator bends prior to interaction with the environment at 24 s. As seen in Fig. 14(b), fluctuations in strain are measured before impact. This is caused by the actuation of the tendons, which results in an axial force on the FBG wire. However, the instant of impact is clearly discernable, as seen by the increase in the measured strain.

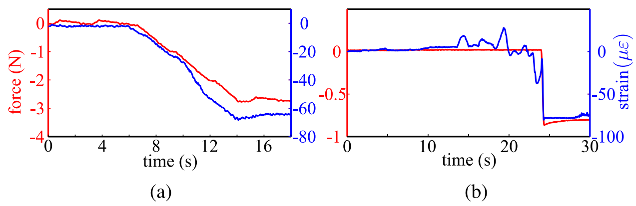

Fig. 14. Interaction of the manipulator tip with a compliant environment. The interaction force is measured by a force sensor, while axial strain in the manipulator is measured by FBG sensors near the tip. Two scenarios are considered: (a) Indentation of the environment without manipulator bending. (b) Steering toward the environment along a reference trajectory. *The accompanying video demonstrates the results of these force sensing experiments.*

VII. Conclusion and Future Work

In this study, we have presented a framework for the control of multisegment continuum manipulators using a modeling approach based on a rigid-link approximation and FBG-based shape sensing. We propose a rigid-link model that describes manipulator shape by a serial chain of rigid-links, connected by flexible rotational joints. As opposed to the constant-curvature approach, the model can account for external loading. Compared with the Cosserat-rod model, which also accounts for external loading, the kinematics of the rigid-link model are simpler such that the manipulator Jacobian can easily be computed. A controller is implemented that uses the manipulator Jacobian to steer the manipulator tip along a reference trajectory while using the kinematic redundancy for obstacle avoidance.

The proposed framework is evaluated using an experimental testbed consisting of a tendon-driven manipulator with two bending segments. An array of 12 FBG sensors is integrated into the manipulator backbone for shape sensing of the manipulator. The controller is evaluated for two experimental cases. The first concerns steering around a static obstacle, while in the second case, an obstacle approaches the manipulator. Closed-loop control results in mean trajectory tracking errors of 0.24 and 0.09 mm with maximum errors of 1.37 and 0.52 mm for Case I and Case II, respectively. In both cases, the manipulator successfully avoids the obstacle.

Finally, we have demonstrated the possibility of measuring interaction force using FBG sensors while simultaneously performing shape sensing. Although promising, force sensing using FBG sensors is challenging and requires further study. Hence, as part of future work, we will investigate using an FBG fiber with a different distribution of FBG sensors, such that manipulator actuation does not affect the measured strains.

In this work, we considered the manipulator to be torsionally stiff and experiments were only performed for the planar case. Therefore, we did not include torsion in the rigid-link model. In future work, we will also consider spatial deformations and the model needs to be extended to account for torsion. This could be done by adding torsional springs to each joint, such that torsion can be described by a rotation around the longitudinal axis of the manipulator.

In our model, we did not consider friction between tendons and tendon guides, which could be a possible source of the error that is observed in the experiments. In future studies, we will consider nonlinear effects, such as friction and hysteresis, and include them into the model. We believe that the rigid-link modeling approach provides insight into the modeling of continuum manipulators, since it can be extended to include manipulator dynamics. In addition, it can account for external loading which is useful when the manipulator interacts with the environment. We did not consider this in the experiments; hence, in future studies, we plan to use the rigid-link model for force sensing and force control.

References

[1] R. J. Webster III and B. A. Jones, "Design and kinematic modeling of constant curvature continuum robots: A review," *Int. J. Robot. Res.*, vol. 29, no. 13, pp. 1661–1683, 2010.

[2] D. B. Camarillo, C. R. Carlson, and J. K. Salisbury, "Task-space control of continuum manipulators with coupled tendon drive," in *Experimental Robotics* (Springer Tracts in Advanced Robotics, vol. 54), O. Khatib, V. Kumar, and G. Pappas, Eds. Berlin, Germany: Springer, 2009, pp. 271–280.

[3] N. Simaan, K. Xu, W. Wei, A. Kapoor, P. Kazanzides, R. Taylor, and P. Flint, "Design and integration of a telerobotic system for minimally invasive surgery of the throat," *Int. J. Robot. Res.*, vol. 28, no. 9, pp. 1134–1153, 2009.

[4] C. Bedell, J. Lock, A. Gosline, and P. E. Dupont, "Design optimization of concentric tube robots based on task and anatomical constraints," in *Proc. IEEE Int. Conf. Robot. Autom.*, Shanghai, China, May. 2011, pp. 398–403.

[5] S. B. Kesner and R. D. Howe, "Position control of motion compensation cardiac catheters," *IEEE Trans. Robot.*, vol. 27, no. 6, pp. 1045–1055, Dec. 2011.

[6] J. Burgner, P. J. Swaney, D. C. Rucker, H. B. Gilbert, S. T. Nill, P. T. Russell, K. D. Weaver, and R. J. Webster, III, "A bimanual teleoperated system for endonasal skull base surgery," in *Proc. IEEE Int. Conf. Intell. Robots Syst.*, San Francisco, CA, USA, Sep. 2011, pp. 2517–2523.

[7] R. E. Goldman, A. Bajo, L. S. MacLachlan, R. Pickens, S. D. Herrell, and N. Simaan, "Design and performance evaluation of a minimally invasive telerobotic platform for transurethral surveillance and intervention," *IEEE Trans. Biomed. Eng.*, vol. 60, no. 4, pp. 918–925, Apr. 2013.

[8] B. A. Jones and I. D. Walker, "Kinematics for multisection continuum robots," *IEEE Trans. Robot.*, vol. 22, no. 1, pp. 43–55, Feb. 2006.

[9] S. Neppalli, M. A. Csencsits, B. A. Jones, and I. D. Walker, "Closed-form inverse kinematics for continuum manipulators," *Adv. Robot.*, vol. 23, pp. 2077–2091, Oct. 2009.

[10] M. W. Hannan and I. D. Walker, "Novel kinematics for continuum robots," in *Advances in Robot Kinematics*. New York, NY, USA: Springer, 2000, pp. 227–238.

[11] M. W. Hannan and I. D. Walker, "Kinematics and the implementation of an elephant's trunk manipulator and other continuum style robots," *J. Robot. Syst.*, vol. 20, no. 2, pp. 45–63, 2003.

[12] P. Sears and P. E. Dupont, "Inverse kinematics of concentric tube steerable needles," in *Proc. IEEE Int. Conf. Robot. Autom.*, Rome, Italy, Apr. 2007, pp. 1887–1892.

[13] R. J. Webster III, J. P. Swensen, J. M. Romano, and N. J. Cowan, "Closed-form differential kinematics for concentric-tube continuum robots with application to visual servoing," in *Experimental Robotics* (Springer Tracts in Advanced Robotics), O. Khatib, V. Kumar, and G. Pappas, Eds. Berlin, Germany: Springer, 2009, pp. 485–494.

[14] D. Trivedi, A. Lotfi, and C. D. Rahn, "Geometrically exact models for soft robotic manipulators," *IEEE Trans. Robot.*, vol. 24, no. 4, pp. 773–780, Aug. 2008.

[15] B. A. Jones, R. L. Gray, and K. Turlapati, "Three dimensional statics for continuum robotics," in *Proc. IEEE Int. Conf. Intell. Robots Syst.*, St. Louis, MO, USA, Oct. 2009, pp. 2659–2664.

[16] D. C. Rucker, B. A. Jones, and R. J. Webster III, "A geometrically exact model for externally loaded concentric-tube continuum robots," *IEEE Trans. Robot.*, vol. 26, no. 5, pp. 769–780, Oct. 2010.

[17] D. C. Rucker and R. J. Webster III, "Computing Jacobians and compliance matrices for externally loaded continuum robots," in *Proc. IEEE Int. Conf. Robot. Autom.*, Shanghai, China, May. 2011, pp. 945–950.

[18] D. C. Rucker and R. J. Webster III, "Deflection-based force sensing for continuum robots: A probabilistic approach," in *Proc. IEEE Int. Conf. Intell. Robots Syst.*, San Francisco, CA, USA, Sep. 2011, pp. 3764–3769.

[19] R. J. Roesthuis, S. Janssen, and S. Misra, "On using an array of fiber Bragg grating sensors for closed-loop control of flexible minimally invasive surgical instruments," in *Proc. IEEE Int. Conf. Intell. Robots Syst.*, Tokyo, Japan, Nov. 2013, pp. 2545–2551.

[20] J. M. Gere and S. P. Timoshenko, *Mechanics of Materials*. Surrey, U.K.: Stanley Thornes, 1999.

[21] R. M. Murray, S. S. Sastry, and L. Zexiang, *A Mathematical Introduction to Robotic Manipulation*, 1st ed. Boca Raton, FL, USA: CRC Press, 1994.

[22] B. Siciliano, L. Sciavicco, L. Villani, and G. Oriolo, *Robotics: Modelling, Planning and Control*. London, U.K.: Springer-Verlag, 2009.

[23] D. B. Camarillo, C. R. Carlson, and J. K. Salisbury, "Configuration tracking for continuum manipulators with coupled tendon drive," *IEEE Trans. Robot.*, vol. 25, no. 4, pp. 798–808, Aug. 2009.

[24] D. Trivedi and C. D. Rahn, "Model-based shape estimation for soft robotic manipulators: The planar case," *J. Mech. Robot.*, vol. 6, p. 021005, 2014.

[25] A. Othonos, K. Kalli, D. Pureaur, and A. Mugnier, "Fibre Bragg gratings," in *Optical Sciences*. New York, NY, USA: Springer-Verlag, 2006, pp. 189–262.

[26] R. J. Roesthuis, M. Kemp, J. J. van den Dobbelsteen, and S. Misra, "Three-dimensional needle shape reconstruction using an array of fiber Bragg grating sensors," *IEEE/ASME Trans. Mechatronics*, vol. 19, no. 4, pp. 1115–1126, Aug. 2014.

[27] D. F. Williams, A. McNamara, and R. M. Turner, "Potential of polyetheretherketone (peek) and carbon-fibre-reinforced peek in medical applications," *J. Mater. Sci. Lett.*, vol. 6, no. 2, pp. 188–190, 1987.

[28] L. Zlajpah and B. Nemec, "Kinematic control algorithms for on-line obstacle avoidance for redundant manipulators," in *Proc. IEEE Int. Conf. Intell. Robots Syst.*, Lausanne, Switzerland, vol. 2, Sep./Oct. 2002, pp. 1898–1903.

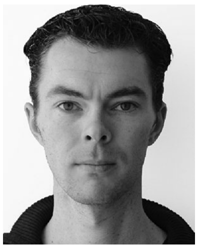

Roy J. Roesthuis (S'11) received the B.Sc. degree in electrical engineering and the M.Sc. degree in mechatronics, both from University of Twente, Enschede, The Netherlands, in 2009 and 2011, respectively, where he is currently working toward the Doctoral degree with the Department of Biomechanical Engineering.

His research interests include robotics for medical procedures.

Sarthak Misra (S'05–M'10) received the Master's degree from McGill University, Montréal, QC, Canada, in 2001, and the Doctoral degree from The Johns Hopkins University, Baltimore, MD, USA, in 2009, both in mechanical engineering.

He is currently a Faculty Member with the Department of Biomechanical Engineering and affiliated with MIRA—Institute for Biomedical Technology and Technical Medicine, University of Twente, Enschede, The Netherlands; and also with the Department of Biomedical Engineering, University of Groningen, Gronigen, The Netherlands, and University Medical Center Groningen. Prior to commencing his studies at The Johns Hopkins University, he was a Dynamics and Controls Analyst on the International Space Station Program for three years. His research interests include surgical robotics and medical microrobotics.

Dr. Misra received the 2014 European Research Council Starting Grant and the 2010 Netherlands Organization for Scientific Research (NWO) VENI Award. He is a Co-Chair of the Robotics and Automation Society Technical Committee on Surgical Robotics and Co-Chair of the International Federation of Automatic Control Technical Committee on Biological and Medical Systems.